Journal of
Materials Chemistry A

PAPER

View Article Online
View Journal | View Issue

Fe-doped and -mediated graphitic carbon nitride nanosheets for enhanced photocatalytic performance under natural sunlight†

Cite this: *J. Mater. Chem. A*, 2014, **2**, 6772

Surendar Tonda,[a] Santosh Kumar,[a] Syam Kandula[b] and Vishnu Shanker*[a]

Herein, we demonstrate the synthesis of highly efficient Fe-doped graphitic carbon nitride (g-C_3N_4) nanosheets *via* a facile and cost effective method. The synthesized Fe-doped g-C_3N_4 nanosheets were well characterized by various analytical techniques. The results revealed that the Fe exists mainly in the +3 oxidation state in the Fe-doped g-C_3N_4 nanosheets. Fe doping of g-C_3N_4 nanosheets has a great influence on the electronic and optical properties. The diffuse reflectance spectra of Fe-doped g-C_3N_4 nanosheets exhibit red shift and increased absorption in the visible light range, which is highly beneficial for absorbing the visible light in the solar spectrum. More significantly, the Fe-doped g-C_3N_4 nanosheets exhibit greatly enhanced photocatalytic activity for the degradation of Rhodamine B under sunlight irradiation. The photocatalytic activity of 2 mol% Fe-doped g-C_3N_4 nanosheets is almost 7 times higher than that of bulk g-C_3N_4 and 4.5 times higher than that of pure g-C_3N_4 nanosheets. A proposed mechanism for the enhanced photocatalytic activity of Fe-doped g-C_3N_4 nanosheets was investigated by trapping experiments. The synthesized photocatalysts are highly stable even after five successive experimental runs. The enhanced photocatalytic performance of Fe-doped g-C_3N_4 nanosheets is due to high visible light response, large surface area, high charge separation and charge transfer. Therefore, the Fe-doped g-C_3N_4 photocatalyst is a promising candidate for energy conversion and environmental remediation.

Received 23rd December 2013
Accepted 6th February 2014

DOI: 10.1039/c3ta15358d

www.rsc.org/MaterialsA

Introduction

Intense research activity has been devoted to searching for active semiconductor photocatalysts, owing to their good performances in the production of renewable energy and environmental remediation.[1,2] Many efficient photocatalysts have been reported for water splitting and environmental remediation. Among them, TiO_2 is the most widely researched semiconductor because of its superior photochemical stability, strong oxidation ability, superhydrophilicity and nontoxicity.[3,4] However, TiO_2 is only able to act as a photocatalyst under ultraviolet light, which accounts for about 4% of sunlight, greatly limiting its practical applications.[5] To utilize solar energy in a more efficient way, the design and development of novel visible light-active photocatalysts is highly in demand, and thus the practical application of such a photocatalytic system has attracted intense efforts.[6–8]

More recently, two-dimensional (2D) graphitic carbon nitride (g-C_3N_4) nanosheets have attracted considerable attention because of their appropriate bandgap, large surface area, and excellent chemical stability, making them potentially suitable for solar energy conversion and environmental remediation. The g-C_3N_4 nanosheets showed superior photocatalytic activity for the degradation of organic pollutants under visible light irradiation.[9,10] However, the efficiency of g-C_3N_4 nanosheets still limits their practical applications due to the high recombination rate of photoinduced electron–hole pairs.[11,12] To resolve this problem, many attempts have been made to improve the efficiency of g-C_3N_4; for example, metal doping (Fe, Zn),[13] metal loading (Ag,[14] Pd[15]), non-metal doping (B,[16] O,[17] S[18]), morphological control,[19,20] and coupling with other semiconductors (Ag_3PO_4,[21] $NaTaO_3$,[22] Fe_3O_4,[23] ZnO,[24] MoS_2,[25] *etc.*) have all been adopted. Among these modifications, doping a metal ion into the semiconductor material is one strategy that can affect the morphology, visible light response and photocatalytic activity. Recently, Fe-doped bulk g-C_3N_4 showed considerable photocatalytic activity for the degradation of Rhodamine B (RhB) as well as the decomposition of water into hydrogen and oxygen.[13] However, the photocatalytic activity of Fe-doped bulk g-C_3N_4 is low due to its low surface area and poor visible light response.

In the present work, we demonstrate a facile and cost effective method to synthesize Fe-doped g-C_3N_4 nanosheets

---

[a] *Department of Chemistry, National Institute of Technology, Warangal-506004, A.P., India. E-mail: vishnu@nitw.ac.in; Fax: +91-870-2459547; Tel: +91-870-2462675*

[b] *Department of Chemistry, Indian Institute of Technology, Roorkee-247667, Uttarakhand, India*

† Electronic supplementary information (ESI) available. See DOI: 10.1039/c3ta15358d

with enhanced photocatalytic performance. The photocatalysts were characterized by powder X-ray diffraction, UV-vis diffuse reflectance spectroscopy, Fourier transform infrared spectroscopy, scanning electron microscopy, transmission electron microscopy, X-ray photoelectron spectroscopy, photoluminescence spectroscopy and elemental analysis. The photodegradation of RhB was employed to evaluate the photocatalytic activities of Fe-doped g-C_3N_4 photocatalysts under sunlight irradiation. Moreover, the stability of the synthesized photocatalysts was also investigated through five successive experimental runs. Based on the experimental results, a possible photocatalytic mechanism for the degradation of RhB over Fe-doped g-C_3N_4 nanosheets under sunlight irradiation was proposed.

Experimental details

Materials

Melamine (Sigma-Aldrich, 99.0%), Rhodamine B (Sigma-Aldrich, 95.0% dye content), eicosane (Sigma-Aldrich, 99.0%), ferric chloride (SRL, 98.0%), terephthalic acid (Merck, AR grade), *tert*-butyl alcohol (Merck, AR grade), ammonium oxalate (Merck, AR grade) and ethanol (SDFCL, 99.9%) were used as received. All other reagents used in this work were of analytically pure grade and used without further purification. All aqueous solutions were prepared with doubly distilled water.

Method

Bulk g-C_3N_4 was synthesized according to the reported procedure.[21] In brief, melamine was heated at 550 °C for 2 h under an N_2 atmosphere with a slow ramp rate for both heating and cooling processes. The obtained yellow colored product was ground to obtain a fine bulk g-C_3N_4 powder. The g-C_3N_4 nanosheets were obtained by liquid exfoliation of the as-synthesized bulk g-C_3N_4 in water. In detail, 0.1 g of bulk g-C_3N_4 powder was dispersed in 250 mL water and then ultrasonicated overnight. The formed suspension was heated at 100 °C to remove water. The resulting pale yellow colored g-C_3N_4 nanosheets are denoted as CN and were used for further study. Finally, Fe-doped g-C_3N_4 nanosheets were synthesized by dissolving an appropriate amount of ferric chloride in 50 mL of acetone. To this solution, 0.5 g of g-C_3N_4 nanosheets were added with stirring, and the resulting suspension was stirred for 2 h at room temperature, centrifuged at about 6000 rpm for 15 min and washed with acetone several times to remove aggregates. The color of the dried samples changed slightly from pale yellow to slightly reddish brown with increasing Fe content. A series of Fe-doped g-C_3N_4 nanosheets were synthesized using different amounts of ferric chloride, and the obtained 0.5, 1, 2 and 3 mol% Fe-doped samples are denoted as FCN-0.5, FCN-1, FCN-2 and FCN-3, respectively.

Characterization

Powder X-ray diffraction (PXRD) patterns were recorded on a Bruker AXS D8 Advance X-ray diffractometer using Ni filtered Cu Kα ($\lambda = 1.5406$ Å) radiation in a 2θ scan range between 10° and 80°. UV-vis diffuse reflectance spectra (UV-vis DRS) were obtained on a THERMO Scientific Evolution 600 diffuse reflectance spectrophotometer, and $BaSO_4$ was used as a reference standard. Fourier transform infrared (FT-IR) spectra were recorded in transmission mode from 4000 to 400 cm^{-1} on a PerkinElmer Spectrum 100 FT-IR spectrophotometer using the KBr pellet technique. Raman studies were carried out on a PerkinElmer RamanStation 400 spectrometer with a 785 nm laser as the excitation source. The composition of the samples was investigated by energy dispersive spectroscopy (SEM-EDS; OXFORD Instruments, INCAx-act). The transmission electron microscopy (TEM) measurements were conducted on an FEI Tecnai G^2 Spirit transmission electron microscope with an acceleration voltage of 200 kV. The chemical compositions of the samples were analyzed by X-ray photoelectron spectroscopy (Kratos Axis ULTRA system incorporating a 165 mm hemispherical electron energy analyzer). The surface area measurements were recorded using a Quanta chrome NOVA 1200e, and the surface areas of the catalysts were estimated using the BET method. UV-visible absorption spectra (UV-vis) were recorded on a THERMO Scientific Evolution 600 UV-Vis NIR spectrophotometer. The photoluminescence (PL) spectra of the photocatalysts were recorded on a TSC Solutions F96pro fluorescence spectrophotometer at an excitation wavelength of 365 nm.

Photocatalytic activity

The photocatalytic activities of the synthesized samples were examined by monitoring the photocatalytic degradation of RhB in aqueous solution under sunlight irradiation. Photocatalytic experiments on the samples were carried out under similar conditions in August 2013 at NIT Warangal, where the fluctuation of the sunlight intensity is minimal during this month. In each experiment, 0.1 g of photocatalyst was added to 250 mL RhB solution with a concentration of 5 mg L^{-1}. Prior to irradiation, the suspensions were magnetically stirred in the dark for 30 min to achieve adsorption equilibrium between the RhB molecules and the photocatalyst. During the sunlight irradiation, the suspensions were periodically withdrawn, centrifuged to separate the photocatalyst and used for absorbance measurements on a UV-vis spectrophotometer. A blank test was also carried out on an aqueous RhB solution without photocatalyst under sunlight irradiation, *i.e.* photolysis of RhB, to evaluate the efficiency of the photocatalyst.

Analysis of reactive species

The effects of various reactive species on the degradation of RhB were examined to understand the photocatalytic mechanism. Various scavengers were added to the RhB solution prior to addition of the photocatalyst. The analysis method was similar to the photodegradation experimental process. Furthermore, the formation of hydroxyl radicals ($^{\bullet}OH$) on the surface of sunlight irradiated photocatalyst was detected by the photoluminescence (PL) technique using terephthalic acid (TA) as a probe molecule. In a brief experimental procedure, 0.1 g of an Fe-doped g-C_3N_4 sample was dispersed in 100 mL of a mixture of a 5×10^{-4} mol L^{-1} aqueous TA solution and a

2×10^{-3} mol L^{-1} NaOH solution at room temperature. The resulting solution was magnetically stirred and the suspension was exposed to sunlight. At 5 min intervals, the suspension was collected and centrifuged to measure the maximum PL intensity using a fluorescence spectrophotometer with an excitation wavelength of 365 nm.

Electrochemical characterization

Electrochemical impedance studies of the synthesized photocatalysts were carried out in a conventional three electrode cell assembly using an electrochemical workstation (Model: IM6e, ZAHNER, GmbH, Germany). The synthesized photocatalyst was used as the working electrode, a platinum wire was used as the counter electrode, and the reference electrode was Ag/AgCl (3 N KCl). All experiments were performed at an open circuit potential of 0.24 V within a frequency range from 10 mHz to 100 kHz with a sinusoidal potential perturbation of ±5 mV amplitude. The data obtained from these studies were analyzed using THALES software. These experiments were carried out in a 10 mM $K_3[Fe(CN)_6]$ solution containing 0.1 M KCl as an electrolyte. The preparation procedures of the working electrodes were as follows: 0.1 g of photocatalyst was mixed with 0.15 g of eicosane ($C_{20}H_{42}$), which is used as a binder at 50 °C. Then, the obtained paste was firmly pressed into a Teflon tube with an inner diameter of 2.5 mm. Finally, the electrode was dried at room temperature for 5 h, and Cu wire was inserted into the electrode for electrical contact.

Results and discussion

Fig. 1a shows the X-ray diffraction patterns of the synthesized bulk g-C_3N_4, and pure and Fe-doped g-C_3N_4 nanosheets. The strong diffraction peak at 27.7° is a characteristic interlayer stacking reflection of conjugated aromatic systems, indexed for g-C_3N_4 as the (002) peak. The small diffraction peak at around 13.2°, indexed as (100), is related to the in-plane structural repeating motif, *i.e.* the hole-to-hole distance of the continuous tri-s-triazine pores.[26] Interestingly, the diffraction patterns of both pure and Fe-doped g-C_3N_4 nanosheets show only the (002) peak. Moreover, the intensity of the (002) peak is significantly decreased and broadened for g-C_3N_4 nanosheets compared to their bulk counterpart.[27] It is also observed that the crystal phase of g-C_3N_4 did not change after doping with Fe, but the diffraction peak position for Fe-doped g-C_3N_4 nanosheets shifted to a slightly higher angle than that of pure g-C_3N_4 nanosheets. However, with increasing Fe content, the peak intensity becomes weaker and the width of the diffraction peak becomes wider, indicating host–guest interactions and an inhibition of polymeric condensation by excess Fe species.[13]

UV-vis diffuse reflectance spectra of the synthesized bulk g-C_3N_4, and pure and Fe-doped g-C_3N_4 nanosheets are shown in Fig. 1b. A slight blue shift is observed for g-C_3N_4 nanosheets compared to their bulk counterpart. Interestingly, the diffuse reflectance spectra of Fe-doped g-C_3N_4 nanosheets exhibit a red shift and increased absorption in the visible light range. With increasing Fe content, the optical band gap gradually shifts to lower energy. Undoubtedly, these results reveal that the Fe ions are indeed incorporated into the lattice of g-C_3N_4, thus altering its electronic structure. The red shift of the absorption wavelength for Fe-doped g-C_3N_4 nanosheets favors the generation of more electron–hole pairs under sunlight irradiation, which can result in enhanced photocatalytic properties. The band gap energy is obtained by plotting $(\alpha h\nu)^2$ *vs.* $h\nu$, where α is the absorption co-efficient and $h\nu$ is the photon energy. The intercept of the tangent to the plot will give a good approximation of the band gap energy. The calculated band gap energies are 2.69, 2.74, 2.65, 2.61, 2.56 and 2.54 eV for bulk g-C_3N_4, CN, FCN-0.5, FCN-1, FCN-2 and FCN-3, respectively.

Fig. 2 shows the FT-IR spectra of the synthesized bulk g-C_3N_4, and pure and Fe-doped g-C_3N_4 nanosheets. The broad absorption band at approximately 3170 cm^{-1}, as shown in Fig. 2, can be assigned to the stretching vibrational modes of residual N–H components associated with uncondensed amino groups.[28] The peak at 1638 cm^{-1} is indexed to stretching vibrational modes, while the bands at 1574, 1411, 1322 and 1245 cm^{-1} are associated with aromatic C–N stretching vibrations.[29,30] The sharp characteristic peak at 808 cm^{-1} corresponds to the s-triazine ring system.[31] From the FT-IR patterns of the Fe-doped g-C_3N_4 nanosheets, it is observed that the intensity of the peaks decreases with increasing Fe content in the Fe-doped g-C_3N_4 nanosheets. It can also be seen that the

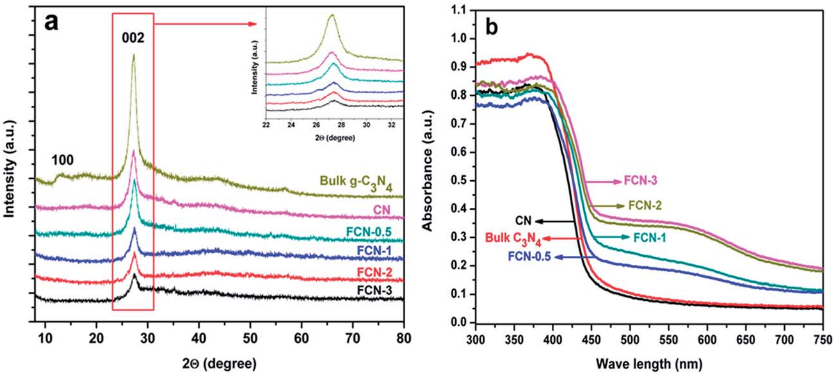

Fig. 1 XRD patterns (a) and UV-vis diffuse reflectance spectra (b) of the synthesized bulk g-C_3N_4, and pure and Fe-doped g-C_3N_4 nanosheets.

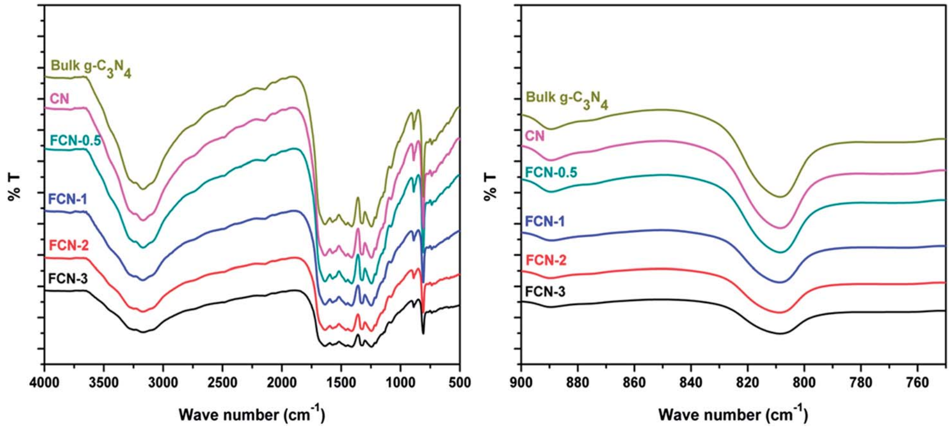

Fig. 2 FT-IR spectra of the synthesized bulk g-C_3N_4, and pure and Fe-doped g-C_3N_4 nanosheets.

main characteristic bands of g-C_3N_4 nanosheets shift to lower wave numbers for the Fe-doped g-C_3N_4 nanosheets. The red shift of the bands suggests that the C–N and C=N bonds are weakened due to interactions between Fe and g-C_3N_4 in the Fe-doped g-C_3N_4 systems.

Fig. 3 shows the Raman spectra of the synthesized bulk g-C_3N_4, pure g-C_3N_4 and Fe-doped g-C_3N_4 (FCN-2) nanosheets recorded with a 785 nm laser as the excitation source. It can be clearly seen that the bulk and pure g-C_3N_4 nanosheets show similar patterns, indicating that the g-C_3N_4 nanosheets retain the same crystal structure as that of bulk g-C_3N_4 after exfoliation. However, the g-C_3N_4 nanosheets show a blue shift of about 5 cm^{-1} compared with bulk g-C_3N_4, which is due to the phonon confinement effect of exfoliated nanosheets, implying their thickness.[27] At the same time, FCN-2 shows a nearly identical Raman pattern but with very low intensity. The Raman peaks observed at approximately 707 and 986 cm^{-1} for all the samples are attributed to the different types of ring breathing modes of s-triazine, which is present in the g-C_3N_4 crystal structure.[32] The above results are in good agreement with the XRD results.

The morphologies of the as-prepared g-C_3N_4 and Fe-doped g-C_3N_4 nanosheets were investigated *via* transmission electron microscopy (TEM). Fig. 4a shows a TEM image of the synthesized pure g-C_3N_4 nanosheets. It can be seen that the TEM image shows free-standing nanosheets with diameters of a few nanometers. The edges of the sheets tend to be ragged in order to minimize their surface area. Furthermore, the selected area electron diffraction (SAED) pattern (Fig. 4b) shows a faint but full diffraction ring which is indexed to the characteristic (002)

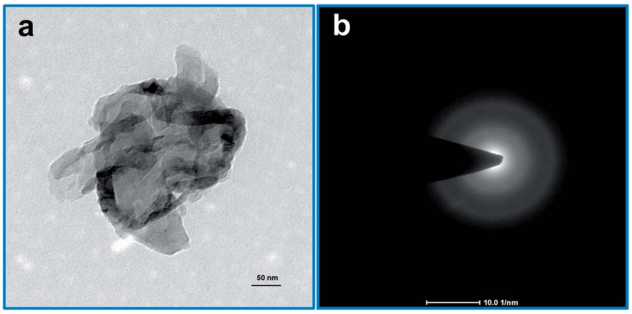

Fig. 4 TEM image of the synthesized CN (a) and the corresponding selected area electron diffraction (SAED) pattern (b).

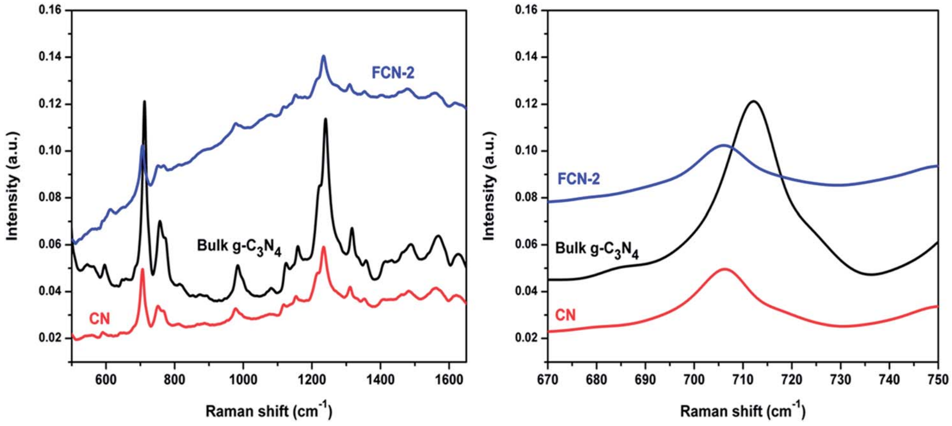

Fig. 3 Raman spectra of the synthesized bulk g-C_3N_4, and pure and Fe-doped g-C_3N_4 nanosheets.

plane of g-C_3N_4.[33] In addition, scanning electron microscopy X-ray energy dispersive spectroscopy (SEM-EDS) was used to determine the chemical compositions of the synthesized samples (Fig. S2 and S3†). The C to N atomic ratios and Fe contents in the Fe-doped g-C_3N_4 nanosheets obtained from the EDS results are listed in Table 1.

The specific surface areas of pure and Fe-doped g-C_3N_4 nanosheets were investigated by nitrogen adsorption isotherm analysis. The specific surface areas of the CN and FCN-2 samples were found to be 358.22 and 365.78 $m^2 g^{-1}$ respectively. A large specific surface area of these nanosheets is useful for better adsorption of organic compounds and also provides more reactive sites for the photocatalytic process, thereby enhancing the photocatalytic activity. X-ray photoelectron spectroscopy (XPS) was performed to determine the chemical composition of the Fe-doped g-C_3N_4 nanosheets and the valance states of various species present therein. Fig. 5a presents the survey scan XPS spectrum of the synthesized Fe-doped g-C_3N_4 nanosheets (FCN-2). The sample contains C, N, and Fe, with sharp photoelectron peaks appearing at binding energies of 288 eV (C 1s), 399 eV (N 1s) and a weak photoelectron peak at 711 eV (Fe 2p).[34,35] The high resolution XPS spectrum (Fig. 5b) of the Fe $2p_{3/2}$ region of the sample indicates that the peak at 710.8 eV can be ascribed to Fe^{3+} ions. The binding energy of 710.8 eV lies within the range of the binding energy of the Fe^{3+} valence state (710.3–711.8 eV),[36] and is close to the reported value.[35] This result confirms that the Fe exists mainly in the +3 oxidation state in Fe-doped g-C_3N_4 samples.

EIS studies

Electrochemical impedance measurements were performed to investigate the charge transfer resistance and the separation efficiency between the photogenerated electrons and holes. Fig. 6a shows the Nyquist plots of bulk g-C_3N_4, pure g-C_3N_4 and Fe-doped g-C_3N_4 (FCN-2) nanosheets. These plots are best fitted by using the equivalent circuit shown in the inset of Fig. 6a. These results demonstrate that the diameter of the semicircle observed for Fe-doped g-C_3N_4 nanosheets is significantly smaller than that observed for bulk g-C_3N_4 and pure g-C_3N_4 nanosheets. The R_{ct} value for Fe-doped g-C_3N_4 nanosheets is low compared with that of bulk g-C_3N_4 and pure g-C_3N_4 nanosheets. This indicates that Fe doping increases the conductivity of g-C_3N_4 significantly. These results demonstrate that the photogenerated electron–hole pairs are more effectively separated in the Fe-doped g-C_3N_4 system, and that there is a more efficient interfacial charge transfer between the electron donor and the electron acceptor, which enhances the photocatalytic activity.[37]

Table 1 Physical and textural properties of the synthesized bulk g-C_3N_4, and pure and Fe-doped g-C_3N_4 nanosheets

Sample	Fe loading (mol%)	Actual Fe loading (from EDS) (mol%)	C/N ratio	Energy gap (eV)
Bulk g-C_3N_4	—	—	0.78	2.69
CN	—	—	0.76	2.74
FCN-0.5	0.5	0.42	0.79	2.65
FCN-1	1	0.85	0.81	2.61
FCN-2	2	1.98	0.83	2.56
FCN-3	3	2.89	0.84	2.54

PL studies

It is widely accepted that enhancement of the photocatalytic activity of a photocatalyst is attributed to efficient photogenerated electron–hole pair separation. Photoluminescence (PL) spectra can be used to investigate the migration, transfer, and recombination processes of the photogenerated electron–hole pairs in a semiconductor.[21,38] Fig. 6b shows the PL spectra of synthesized bulk g-C_3N_4, and pure and Fe-doped g-C_3N_4 nanosheets recorded at room temperature with an excitation wavelength of 365 nm. As can be seen from this figure, the PL spectra of pure and Fe-doped g-C_3N_4 nanosheets show a slight blue shift compared with that of bulk g-C_3N_4. The blue shift of the PL spectra and the band gaps can be ascribed to the quantum confinement effect, with the conduction and valence bands shifting in opposite directions.[27] From the figure, it is also observed that there is a significant decrease in the PL intensity of Fe-doped g-C_3N_4 nanosheets compared to that of bulk g-C_3N_4 and pure g-C_3N_4 nanosheets. The weak intensity PL signal represents a lower recombination probability of photogenerated charge carriers. Therefore, introduction of Fe species on the surface of g-C_3N_4 could effectively inhibit the recombination of photogenerated charge carriers, which is useful for greater separation of photogenerated electron–hole pairs in g-C_3N_4. The maximum PL quenching is observed for FCN-2, which may be due to the improved photogenerated charge transfer between the Fe and g-C_3N_4.

Photocatalytic performance

The photocatalytic activities of the synthesized bulk g-C_3N_4, and pure and Fe-doped g-C_3N_4 nanosheets were evaluated for the degradation of RhB under sunlight irradiation, as shown in Fig. 7a. The photolysis of RhB under the same experimental conditions (without catalyst) indicates that RhB is stable under sunlight irradiation (Fig. S4†). Moreover, the adsorption ability of FCN-2 was also investigated in the dark for the same duration (Fig. S5†). These results indicate that both light and catalyst are necessary for an efficient photocatalytic degradation reaction. The synthesized Fe-doped g-C_3N_4 nanosheets exhibit a much higher photocatalytic activity than bulk g-C_3N_4 and pure g-C_3N_4 nanosheets. The photocatalytic results also demonstrate that the doping amount of Fe has a strong influence on the photodegradation of RhB. Thus, the optimal Fe content in g-C_3N_4 nanosheets is 2 mol%, and then the photocatalytic activity decreases with increasing Fe content. The decrease in the photocatalytic activity can be explained by the fact that excess Fe species may act as recombination centers for photo-induced electrons and holes and/or cover the active sites on the g-C_3N_4 surface and thereby reduce the efficiency of charge separation.[14] Therefore, the order of photocatalytic activity of the synthesized samples for the degradation of RhB under sunlight irradiation is summarized as follows: FCN-2 > FCN-1 > FCN-3 > FCN-0.5 >

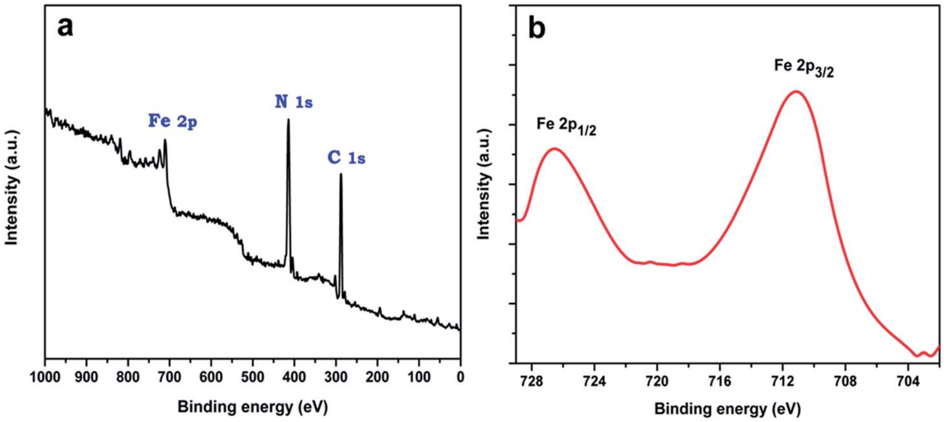

Fig. 5 XPS spectra of the synthesized Fe-doped g-C_3N_4 nanosheets: (a) survey spectrum and (b) Fe 2p spectrum.

CN > bulk g-C_3N_4. The corresponding first-order kinetics plot shown in Fig. 7b indicates that the 2 mol% Fe-doped g-C_3N_4 nanosheets exhibit the highest degradation rate, which is almost 7 times higher than that of bulk g-C_3N_4 and 4.5 times higher than that of pure g-C_3N_4 nanosheets.

Reaction mechanism

Reactive species. To investigate the photocatalytic mechanism for the degradation of RhB under sunlight irradiation over Fe-doped g-C_3N_4 nanosheets, the influence of the main reactive species, including hydroxyl radicals ($^•OH$), superoxide anion radicals ($O_2^{•-}$) and holes (h^+), on the photodegradation process was explored. To examine the role of these reactive species, different scavengers, namely ammonium oxalate (AO) for h^+, *tert*-butyl alcohol (TBA) for $^•OH$ and N_2 for $O_2^{•-}$, were employed in this study. From Fig. 8a, it can be seen that the photocatalytic conversion of RhB decreases most rapidly after N_2 purging. This means that dissolved O_2 is a key factor in RhB photodegradation in the case of the Fe-doped g-C_3N_4 (FCN-2) photocatalyst, affecting the formation of $O_2^{•-}$ *via* direct reduction of O_2 and the formation of $^•OH$ *via* multistep reduction of O_2.[16] On addition of AO, the rate of photocatalytic degradation of RhB is drastically reduced compared with no scavenger under the same conditions. In addition, a significant change in the degradation of RhB is observed after the addition of TBA, which indicates that photogenerated $O_2^{•-}$, $^•OH$ and h^+ play an important role in the degradation of RhB.

Hydroxyl radical generation. The $^•OH$ radical generation during the photocatalytic reaction can be easily detected by a photoluminescence (PL) technique using terephthalic acid (TA) as a probe molecule, which readily reacts with $^•OH$ to produce the highly fluorescent product, 2-hydroxyterephthalic acid. From Fig. 8b, it can be seen that the maximum intensity peaks in the PL spectra were observed at approximately 435 nm at an excitation wavelength of 365 nm, demonstrating that $^•OH$ is formed in the photocatalytic oxidation process, which is in agreement with the results of TBA quenching. From Fig. 8b, it is also observed that the PL intensity increases gradually with increasing irradiation time, which demonstrates that $^•OH$ is indeed generated on the sunlight irradiated surface of Fe-doped g-C_3N_4 nanosheets. From the results above, it is clear that the $^•OH$ radicals only originate from the reaction of photogenerated electrons during the multistep reduction of dissolved O_2.

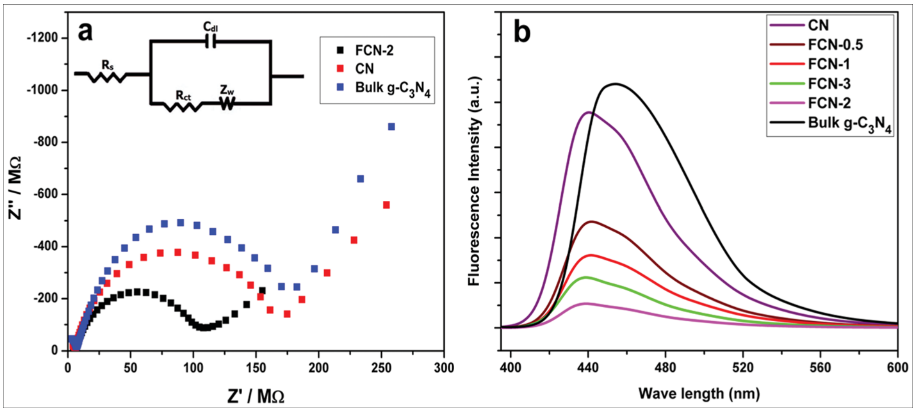

Fig. 6 (a) EIS profiles of the synthesized bulk g-C_3N_4, and pure and Fe-doped g-C_3N_4 nanosheets and (b) room temperature photoluminescence (PL) spectra of the synthesized bulk g-C_3N_4, and pure and Fe-doped g-C_3N_4 nanosheets excited at 365 nm.

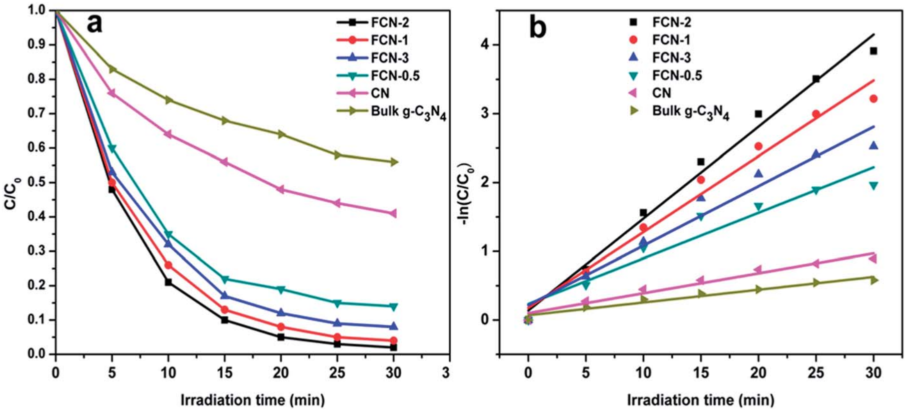

Fig. 7 (a) Comparison of the photocatalytic activities of bulk g-C_3N_4, and pure and Fe-doped g-C_3N_4 nanosheets for the degradation of RhB in aqueous solution under sunlight irradiation and (b) the corresponding first-order kinetics plots of bulk g-C_3N_4, and pure and Fe-doped g-C_3N_4 nanosheets.

Proposed mechanism. Based on our experimental results, a possible photocatalytic mechanism was proposed for the enhanced photocatalytic activity of Fe-doped g-C_3N_4 nanosheets, as shown in Fig. 9. The doped Fe^{3+} can act as a temporary photogenerated electron and hole trapping site, which can facilitate the separation of photogenerated charge carriers and promotes the interfacial electron transfer process. This is due to the fact that the reduction potential of Fe^{3+}/Fe^{2+} (+0.40 V *vs.* NHE) lies between the conduction band (CB) and the valence band (VB) of g-C_3N_4.[39] The photogenerated electrons excited to the CB of g-C_3N_4 under sunlight irradiation are trapped by the Fe^{3+} species, which was confirmed by photoluminescence studies. These trapped electrons can react with electron acceptors present in the system, such as O_2, reducing it to $O_2^{\bullet -}$. Meanwhile, valance holes generated on the surface of g-C_3N_4 can oxidize OH^- or H_2O molecules to $^{\bullet}OH$ using Fe^{3+} as a mediator. In addition to g-C_3N_4-mediated degradation, dye degradation can proceed *via* sensitization, *i.e.* injection of electrons from the dye molecules into the conduction band of g-C_3N_4 as RhB absorbs 554 nm light, which further enhances the separation efficiency of the charge carrier.[40] Thus, charge carrier transfer is improved and recombination of photogenerated electron–hole pairs is inhibited by Fe^{3+} doping. It is also observed that there is a tendency to transfer the charge carriers from Fe^{2+} or Fe^{4+} to regenerate Fe^{3+}, which may be due to the high stability of Fe^{3+} compared to Fe^{2+} and Fe^{4+}.[41] Therefore, $O_2^{\bullet -}$ and h^+ are the main reactive species in the degradation of RhB, which was also confirmed by the scavenger test.

Reusability

The photostability and reusability of a photocatalyst are also very important for practical applications. To evaluate the stability and reusability of Fe-doped g-C_3N_4 nanosheets, five successive photocatalytic experimental runs were carried out by adding recycled FCN-2 photocatalyst to fresh RhB solutions with no change in the overall concentration of the catalyst under sunlight irradiation. As shown in Fig. 10, the photocatalytic activity of FCN-2 for the degradation of RhB does not significantly decrease after five successive experimental runs under the same experimental conditions. The XRD pattern

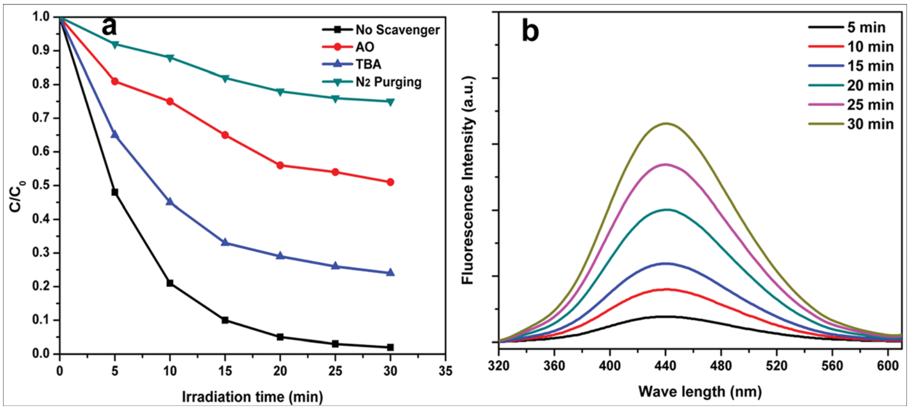

Fig. 8 (a) Effects of different scavengers on the degradation of RhB under sunlight irradiation in the presence of the FCN-2 photocatalyst and (b) $^{\bullet}OH$ trapping PL spectra of FCN-2 in TA solution under sunlight irradiation.

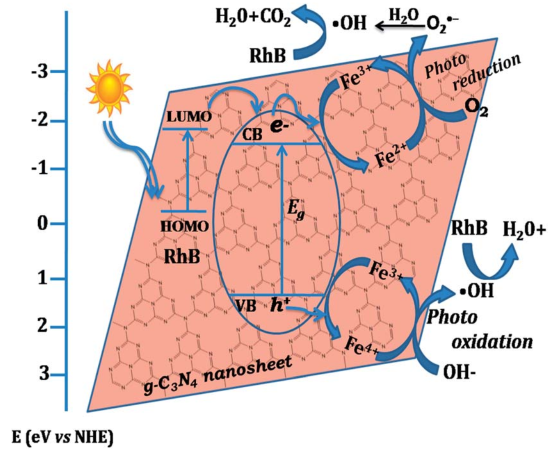

Fig. 9 Schematic illustration of the high photocatalytic activity of Fe-doped g-C_3N_4 nanosheets for the degradation of RhB in aqueous solution under sunlight irradiation.

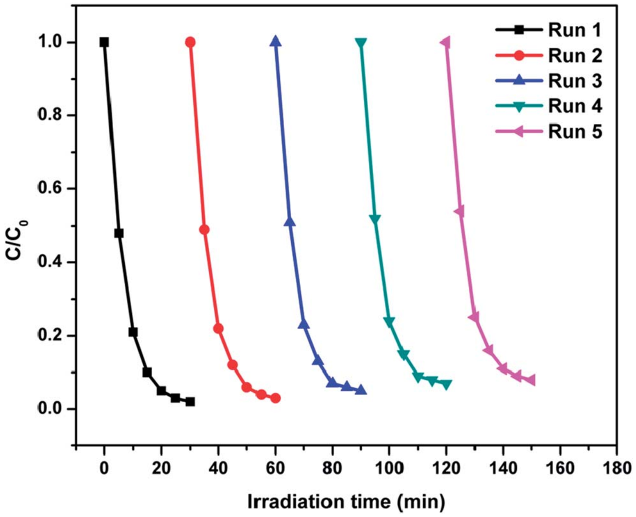

Fig. 10 Reusability of the FCN-2 photocatalyst for the photocatalytic degradation of RhB during five successive experimental runs in aqueous solution under sunlight irradiation.

(Fig. S6†) of reused FCN-2 indicates that Fe-doped g-C_3N_4 nanosheets possess high structural stability and retain more than 90% efficiency even after five successive experimental runs. These results indicate that Fe^{3+} ions are tightly bound on the surface of the electron-rich g-C_3N_4 structure, mainly through Fe–N bonds.[13] Therefore, Fe-doped g-C_3N_4 nanosheets can be used as a reusable photocatalyst with improved photocatalytic activity for practical applications in environmental protection.

Conclusion

In summary, highly efficient Fe-doped g-C_3N_4 nanosheets were successfully synthesized *via* a simple and cost effective method. The Fe species were determined to be in the +3 oxidation state in the Fe-doped g-C_3N_4 nanosheets. The Fe-doped g-C_3N_4 nanosheets exhibited enhanced photocatalytic activity for the degradation of RhB under sunlight irradiation. Fe doping enhanced the light absorption in the visible region by narrowing the band gap. Additionally, the trapping experiments confirmed that photogenerated $O_2^{•-}$, $^•OH$ and h^+ are responsible for photodegradation in the Fe-doped g-C_3N_4 nanosheet system. Moreover, the synthesized photocatalysts were highly stable even after five successive experimental runs, without any obvious change in the activity. The present work demonstrates the feasibility of using Fe as an efficient mediator to improve the photocatalytic performance of the g-C_3N_4 system, which has tremendous potential for practical applications.

Acknowledgements

The authors thank the Department of Science and Technology, Government of India for financial support (SR/FT/CS-096/2009).

References

1 X. B. Chen, S. H. Shen, L. J. Guo and S. S. Mao, *Chem. Rev.*, 2010, **110**, 6503–6570.
2 A. Kudo and Y. Miseki, *Chem. Soc. Rev.*, 2009, **38**, 253–278.
3 X. Chen and S. S. Mao, *Chem. Rev.*, 2007, **107**, 2891–2959.
4 P. V. Kamat, *J. Phys. Chem. C*, 2012, **116**, 11849–11851.
5 M. Shang, W. Wang, S. Sun, L. Zhou and L. Zhang, *J. Phys. Chem. C*, 2008, **112**, 10407–10411.
6 L. Zhang and Y. Zhu, *Catal. Sci. Technol.*, 2012, **2**, 694–706.
7 G. H. Tian, Y. J. Chen, W. Zhou, K. Pan, Y. Z. Dong, C. G. Tian and H. G. Fu, *J. Mater. Chem.*, 2011, **21**, 887–892.
8 F. Zuo, L. Wang, T. Wu, Z. Y. Zhang, D. Borchardt and P. Y. Feng, *J. Am. Chem. Soc.*, 2010, **132**, 11856–11857.
9 N. Cheng, J. Tian, Q. Liu, C. Ge, A. H. Qusti, A. M. Asiri, A. O. Al-Youbi and X. Sun, *ACS Appl. Mater. Interfaces*, 2013, **5**, 6815–6819.
10 P. Niu, L. Zhang, G. Liu and H. M. Cheng, *Adv. Funct. Mater.*, 2012, **22**, 4763–4770.
11 S. B. Yang, Y. J. Gong, J. S. Zhang, L. Zhan, L. L. Ma, Z. Y. Fang, R. Vajtai, X. C. Wang and P. M. Ajayan, *Adv. Mater.*, 2013, **25**, 2452–2456.
12 X. F. Chen, J. S. Zhang, X. Z. Fu, M. Antonietti and X. C. Wang, *J. Am. Chem. Soc.*, 2009, **131**, 11658–11659.
13 X. C. Wang, A. Thomas, X. Z. Fu and M. Antonietti, *Adv. Mater.*, 2009, **21**, 1609–1612.
14 L. Ge, C. C. Han, J. Liu and Y. F. Li, *Appl. Catal., A*, 2011, **409–410**, 215–222.
15 C. Chang, Y. Fu, M. Hu, C. Wang, G. Shan and L. Zhu, *Appl. Catal., B*, 2013, **142–143**, 553–560.
16 S. C. Yan, Z. S. Li and Z. G. Zou, *Langmuir*, 2010, **26**, 3894–3901.
17 J. H. Li, B. Shen, Z. H. Hong, B. Z. Lin, B. F. Gao and Y. L. Chen, *Chem. Commun.*, 2012, **48**, 12017–12019.
18 G. Liu, P. Niu, C. H. Sun, S. C. Smith, Z. G. Chen, G. Q. Lu and H. M. Cheng, *J. Am. Chem. Soc.*, 2010, **132**, 11642–11648.
19 X. Bai, L. Wang, R. Zong and Y. Zhu, *J. Phys. Chem. C*, 2013, **117**, 9952–9961.

20 J. H. Sun, J. S. Zhang, M. Z. Zhang, M. Antonietti, X. Z. Fu and X. C. Wang, *Nat. Commun.*, 2012, 1139–1144.

21 S. Kumar, T. Surendar, A. Baruah and V. Shanker, *J. Mater. Chem. A*, 2013, **1**, 5333–5340.

22 S. Kumar, B. Kumar, T. Surendar and V. Shanker, *Mater. Res. Bull.*, 2014, **49**, 310–318.

23 S. Kumar, T. Surendar, B. Kumar, A. Baruah and V. Shanker, *J. Phys. Chem. C*, 2013, **117**, 26135–26143.

24 Y. J. Wang, R. Shi, J. Lin and Y. F. Zhu, *Energy Environ. Sci.*, 2011, **4**, 2922–2929.

25 Y. D. Hou, A. B. Laursen, J. S. Zhang, G. G. Zhang, Y. S. Zhu, X. C. Wang, S. Dahl and I. Chorkendorff, *Angew. Chem., Int. Ed.*, 2013, **52**, 3621–3625.

26 F. Goettmann, A. Fischer, M. Antonietti and A. Thomas, *Angew. Chem., Int. Ed.*, 2006, **45**, 4467–4471.

27 X. Zhang, X. Xie, H. Wang, J. Zhang, B. Pan and Y. Xie, *J. Am. Chem. Soc.*, 2013, **135**, 18–21.

28 G. Zhang, J. Zhang, M. Zhang and X. Wang, *J. Mater. Chem.*, 2012, **22**, 8083–8091.

29 L. Liu, D. Ma, H. Zheng, X. J. Li, M. J. Cheng and X. H. Bao, *Microporous Mesoporous Mater.*, 2008, **110**, 216–222.

30 X. F. Li, J. Zhang, L. H. Shen, Y. M. Ma, W. W. Lei, Q. L. Cui and G. T. Zou, *Appl. Phys. A: Mater. Sci. Process.*, 2009, **94**, 387–392.

31 Y. G. Li, J. A. Zhang, Q. S. Wang, Y. X. Jin, D. H. Huang, Q. L. Cui and G. T. Zou, *J. Phys. Chem. B*, 2010, **114**, 9429–9434.

32 P. V. Zinin, L. C. Ming, S. K. Sharma, V. N. Khabashesku, X. Liu, S. Hong, S. Endo and T. Acosta, *Chem. Phys. Lett.*, 2009, **472**, 69–73.

33 L. Fang, H. Ohfuji, T. Shinmei and T. Irifune, *Diamond Relat. Mater.*, 2011, **20**, 819–825.

34 X. F. Li, J. Zhang, L. H. Shen, Y. M. Ma, W. W. Lei, Q. L. Cui and G. T. Zou, *Appl. Phys. A: Mater. Sci. Process.*, 2009, **94**, 387–392.

35 J. Yu, Q. Xiang and M. Zhou, *Appl. Catal., B*, 2009, **90**, 595–602.

36 (*a*) J. F. Moulder, W. F. Stickle, P. E. Sobol and K. D. Bomben, *Handbook of X-ray Photoelectron Spectroscopy*, ed. J. Chastain, Perkin-Elmer, Eden Prairie, MN, 1992; (*b*) T. Choudbury, S. O. Saied, J. L. Sullivan and A. M. Abbot, *J. Phys. D: Appl. Phys.*, 1989, **22**, 1185–1195.

37 L. Huang, H. Xu, Y. Li, H. Li, X. Cheng, J. Xia, Y. Xu and G. Cai, *Dalton Trans.*, 2013, **42**, 8606–8616.

38 T. Surendar, S. Kumar and V. Shanker, *Phys. Chem. Chem. Phys.*, 2014, **16**, 728–735.

39 X. Chen, J. Zhang, X. Fu, M. Antonietti and X. Wang, *J. Am. Chem. Soc.*, 2009, **131**, 11658–11659.

40 L. Xu, E. M. P. Steinmiller and S. E. Skrabalak, *J. Phys. Chem. C*, 2012, **116**, 871–877.

41 J. Yu, Q. Xiang and M. Zhou, *Appl. Catal., B*, 2009, **90**, 595–602.